Heat Treatment Conditions for High-Performance High-Pressure Die-Cast Al–Si–Cu–Mg Alloy

Hüseyin Demirtaş, Erdem Karakulak,* and Nadendla Hari Babu

Random porosity in high-pressure die castings of aluminum alloys poses additional challenges in the form of blistering during follow-on heat treatment process. To avoid blisters, the current industrial practice is to lower solution temperature, but this compromises the strength. Herein, kinetics of eutectic Si spheroidization and coarsening during various solution treatment conditions and maximizing the dissolution of much needed Al_2Cu and $Al_5Cu_2Mg_8Si_6$ phases, followed by formation of their precipitates in the aging stage with higher particle number densities, are studied and then higher tensile strength of 435 MPa in most commonly used high-pressure die-cast Al–Si–Cu–Mg alloy without causing blisters is demonstrated.

1. Introduction

The need to reduce fuel consumption and CO_2 emissions leads to lighter vehicle design, which causes a requirement for parts with thinner wall sections made out of high-strength materials.[1,2] Al–Si alloys possess a high strength-to-weight ratio, high corrosion resistance, good castability, and machinability.[3] These alloys can be produced with different casting processes like sand casting, low-pressure die casting, permanent mould casting, etc. High-pressure die casting (HPDC) is the most applied casting method for producing thin-walled cast parts with high productivity. HPDC provides low cycle times, high cooling rates, high surface quality, and near-net shape castings.[4–6] Worldwide, HPDC accounts for approximately half of all aluminum castings and is commonly used for manufacturing automotive components and other consumer products.[7]

The addition of other alloying elements like Cu and Mg makes these Al–Si alloys heat treatable. Yield strength of Al–Si–Cu–Mg

H. Demirtaş
TOBB Technical Science Vocational School
Karabuk University
78000 Karabuk, Turkey

E. Karakulak, N. H. Babu
BCAST
Brunel University London
Kingston Lane, Uxbridge, Middlesex UB8 3PH, UK
E-mail: erdem.karakulak@brunel.ac.uk

The ORCID identification number(s) for the author(s) of this article can be found under https://doi.org/10.1002/adem.202301196.
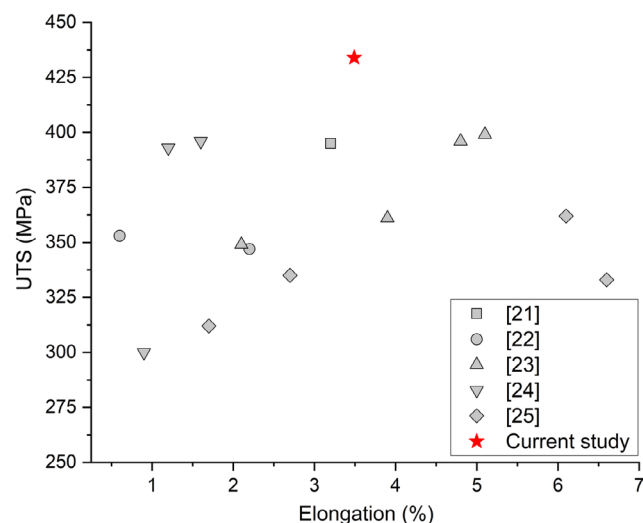
HPDC alloys can be increased with heat treatments from 160 to over 300 MPa, whereas ultimate tensile strength can reach as high as 400 MPa.[8,9] A comparison of the mechanical properties of heat-treated HPDC alloys with similar chemical compositions gathered from the published literature and the current study is shown in **Figure 1**. Applied heat treatment includes solution treatment at high temperature (480–525 °C), water quenching, and natural or artificial aging (150–240 °C).[10] The objectives of the solution treatment are to dissolve the maximum amount of intermetallics to obtain a supersaturated solid solution after quenching and to convert the acicular morphology of eutectic Si particles to a spherical morphology.[11–14] Solution treatment temperature and duration are critical parameters to obtain desired mechanical properties. Higher temperatures and longer durations allow more solute to dissolve in the α-Al matrix. However, increasing the temperature above a limit can cause incipient melting. To prevent this, the temperature should not exceed the melting point of the last solidified phase in the microstructure.[15,16] Prolonged solution treatment durations can cause coarsening of grains and Si particles, which would decrease the number density of these particles and affect the mechanical properties negatively. In the case of HPDC castings, high temperatures and longer durations can cause another problem called blistering. During the HPDC process, the melt is injected into the die cavity to fill thin sections of the casting. This causes a melt flow with extreme turbulence and ends up with entrapment of gas in the solidified part.[7] Also vapor formed by decomposition of die lubricants can cause porosity in the HPDC castings.[17] At elevated temperatures during solution treatment, the gas inside the casting starts to expand, if the gas porosity is close enough to the surface, the stress can plastically deform the overlying surface layer to form blisters.[18] Formation of blisters can cause cast parts to be scrapped and reduce productivity.[19] Because of this problem, heat treatments of HPDC parts are problematic and usually lower temperatures and/or shorter durations are selected.[20]

In the case of Al–Si–Cu–Mg alloys, the intermetallics that can be formed are mainly Al_2Cu (θ), Mg_2Si, and $Al_5Cu_2Mg_8Si_6$ (Q) phases.[21] Formation of these intermetallics depends on the Cu/Mg ratio; it was reported based on the thermodynamic calculations for a similar alloy that the formation of the Mg_2Si phase is not possible when the Cu/Mg ratio is more than 0.65.[22] Vanderslius et al.[23] reported near-complete dissolution of θ and Q phases in 1 h at 495 °C for a similar alloy (B319) cast into a preheated permanent mould. Compared to HPDC process, the

**ADVANCED
SCIENCE NEWS**

www.advancedsciencenews.com

**ADVANCED
ENGINEERING
MATERIALS**

www.aem-journal.com

Figure 1. Comparison of mechanical properties of heat-treated HPDC Al–Si–Cu–Mg alloys.[40–44]

cooling rate of the sample in the mentioned study was very slow (0.17 °C s^{-1}), which causes formation of a coarser grain structure. Almost complete dissolution of θ phase at 500 °C in 30 min was also reported by Sadeghi et al. for an alloy containing 2.8% Cu and 0.5% Mg with a secondary dendritic arm spacing value similar to the HPDC-cast samples. Although incomplete dissolution of Q phase was stated in the same study, its quick dissolution in the first 30 min of the heat treatment was mentioned.[24] In terms of silicon morphology, experimental results reported by Timelli et al. showed that 15 min at 475 °C is enough for spheroidization of Si particles in a Sr-modified, HPDC-cast AlSi7MgMn alloy.[25]

This manuscript investigates the heat treatment conditions under which higher strength can be achieved without causing blistering in high-pressure die-cast Al–Si–Cu–Mg alloy system (with and without Sr modification). The main investigation is focused on exploring optimal conditions to achieve desirable morphology of eutectic Si through studying the growth kinetics and maximizing the dissolution of much-needed Al_2Cu and $Al_5Cu_2Mg_8Si_6$ phases, followed by formation of their precipitates in the aging stage with higher particle number densities.

2. Experimental Section

Commercial A384 ingots with the composition listed in **Table 1** and Al–10Sr master alloy rods were used as raw materials to
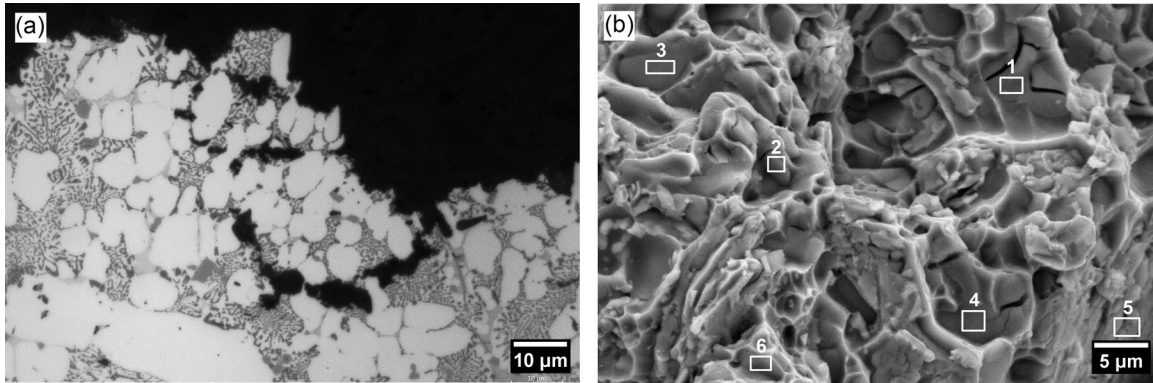
produce A384 and A384 + Sr alloys. These ingots were melted in clay bonded graphite crucibles using electrical resistance furnaces. Rotary degassing was applied to the melt at 740 °C for 10 min; the head rotation speed and argon gas flow were selected as 350 rpm and 4 L min^{-1}, respectively. Casting temperature was chosen as 710 °C, and samples were cast using a 4500 kN cold chamber HPDC machine. 8 ASTM B557 tensile samples with a gauge length and diameter of 50 and 6.35 mm, respectively, were cast in each shot; further information about the geometry of the cast samples can be found elsewhere.[26] An optical emission spectrometer (Oxford Instruments Foundry-Master Pro) was used to analyze the chemical composition of the investigated alloys; the results of the chemical analyses are shown in Table 1.

Heat treatments were conducted using electrical resistance furnaces. The spatial variation of the temperature was measured to be ±2 °C. Quenching was performed in room-temperature water after solution heat treatment. Samples were solution treated at different temperatures varied from 470 to 530 °C for three different durations namely 30, 60, and 120 min. For artificial aging, two different aging temperatures were selected as 170 and 190 °C, and artificial aging was conducted up to 14 h. Some of the samples were kept at room temperature for 14 days after solution treatment and quenching to obtain T4 condition. The aging was conducted in an oven where the temperature was precisely controlled. Hardness of the heat treated samples was measured to obtain optimum heat treatment conditions; a Buehler Vickers microhardness tester was used with a 500 g load and 10 s dwell time. All reported hardness values were an average of 10 measurements. All the tensile tests were conducted at room temperature using a 50 mm extensometer and 1 mm min^{-1} extension rate in Instron 5500 Universal tester. At least three samples were tested for each condition to obtain an average value. Zeiss optical microscope, Jeol JCM 6000Plus, and Carl Zeiss Ultra Plus Gemini field emission scanning electron microscope (FESEM) equipped with energy-dispersive X-ray spectroscopy (EDX) were used for microstructural investigations. ImageJ software was used to analyze the selected microstructure images to understand the evolution of the microstructural constituents with different heat treatments. Themo-Calc software was used to calculate the volume fractions of the phases formed during solidification.

3. Results

3.1. As-Cast Condition

To understand the fracture mode of the materials, fracture surfaces of the as-cast (F) tensile test specimens were investigated

Table 1. Chemical composition of alloys.

	Al [wt%]	Si [wt%]	Cu [wt%]	Ni [wt%]	Sr [wt%]	Mg [wt%]	Mn [wt%]	Fe [wt%]	Others [wt%]
ASM A384[a]	Bal.	10.5–12	3–4.5	Max 0.5	–	0.1 (max)	0.5 (max)	1.3 (max)	
A384	Bal.	12.00	4.11	0.01	–	0.32	0.21	0.86	<0.2
A384 + Sr	Bal.	11.70	3.92	0.01	0.02	0.32	0.21	0.84	<0.2

[a]Standard chemical composition of A384 alloy.[45]

**ADVANCED
SCIENCE NEWS**

www.advancedsciencenews.com

**ADVANCED
ENGINEERING
MATERIALS**

www.aem-journal.com

Figure 2. Microstructures of A384 in as-cast condition: a) optical image showing cross section of the fracture surface and b) SEM image of perpendicular section showing cracks along the intermetallics and Si particles.

and spread of the cracks in the microstructure and the rupture surface are shown in **Figure 2**. The primary and secondary cracks were observed to spread along the intergranular paths where brittle intermetallics, as well as the acicular Si phases are located. It is clear from the microstructure that the ductile α-Al matrix surrounding these brittle phases prevents crack propagation by deflecting or bridging the crack and blinding the crack tip. As shown in Figure 2b, cracks originate within intermetallic and Si phases and propagate through the interdendritic regions, and finally the α-Al phase fractures after some plastic deformation (Figure 2a).

EDX analyses (**Table 2**) of the faceted surfaces reveal that they are mostly fractured Si particles, and some are intermetallics. It is established that the amount of fractured silicon particles for the modified alloy was significantly lower than the unmodified alloy due to a lower aspect ratio and finer particle size.[27] The main subject of this study is focused on investigation of the kinetics of Si phase during heat treatment to obtain desirable morphology that leads to reduced cracking.

3.2. Solution Heat Treatments

During solution treatment, the unmodified eutectic Si particle branches disintegrate, and the disintegration time (t_{max}) is given by

$$t_{max} = \frac{32\pi^2}{9} * \frac{kT}{D_s\gamma} * \left(\frac{\rho}{\phi}\right)^4 * \ln\frac{\rho}{\phi} \tag{1}$$
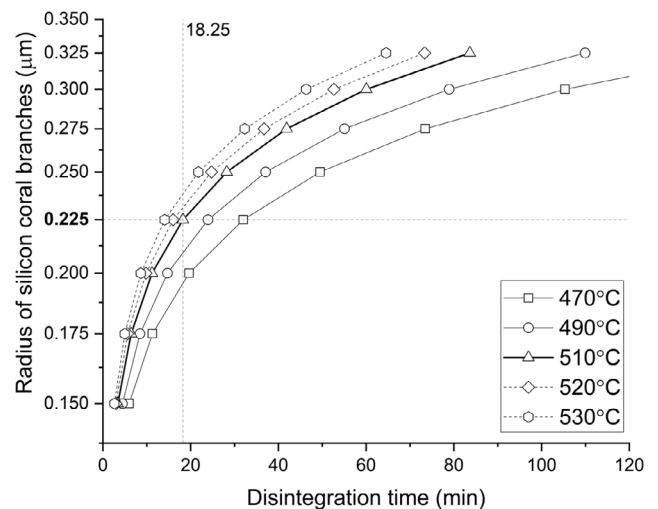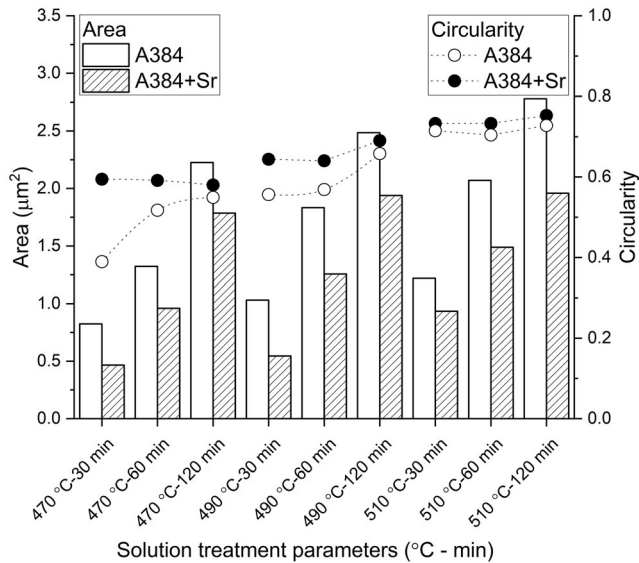
$$D_s = D_0 * \exp\left(-\frac{E_{A,inter} - E_{A,v}}{RT}\right) \tag{2}$$

where $E_{A,inter}$ denotes the activation energy for interdiffusion of Si in Al (148.6 kJ mol^{-1}), $E_{A,v}$ is the activation energy of vacancy formation in Al (74.3 kJ mol^{-1}), R is the universal gas constant (8.314 J mol^{-1} K^{-1}), T is the temperature (K), k is the Boltzmann constant (1.38 × 10^{-23} J K^{-1}), γ is the interfacial energy of Al–Si interface (1 Jm^{-2}), ϕ is the covalent atomic diameter of Si (2.22 × 10^{-10} m), ρ is the Si particle radius, D_s is the diffusion coefficient, and D_0 is the frequency factor (2.29 × 10^{-4} m^{2}s^{-1}).[28]

Figure 3 shows the calculated disintegration time for a given Si branch size. The higher the heat treatment temperature, the shorter the time needed to disintegrate the branches. The measured width of the silicon particles in the cast samples varied in the range of 0.2–1 µm (Figure 6a) with a mean value of 0.45 µm. If the average branch radius is selected as 0.225 µm from Figure 3, the theoretical disintegration time is 18.25 min at 510 °C. For the same silicon particle size, the time needed for disintegration increases to 25 min at 490 °C and 35 min at 470 °C. This value corroborates with the observed experimental

Table 2. EDX analyses (atomic%) of the phases on the fracture surface.

Point	Al	Si	Fe	Ni	Cu
1	25.5	72.51	0.46	0.34	1.2
2	34.78	63.75	0.01	0.28	1.17
3	15.8	83.12	–	0.32	0.77
4	17.2	81.88	–	0.19	0.72
5	70.78	6.55	18.38	0.89	3.41
6	25.71	72.54	0.17	0.38	1.19

Figure 3. Relationship between the radius of silicon coral branches (ρ) and disintegration time (t_{max}) for various temperatures.

ADVANCED
SCIENCE NEWS
www.advancedsciencenews.com

ADVANCED
ENGINEERING
MATERIALS
www.aem-journal.com

Figure 4. Average area and circularity values of eutectic Si phase after different solution treatments.

results as shown in **Figure 4**. Even though the calculated disintegration time for Si particles at 510 °C is less than 20 min, experiments showed that it was not enough for all particles to disintegrate and spheroidize. The disintegration time is calculated using the average branch radius of Si particles. The actual sizes of the Si particles in the cast samples are different from this average value; thus, more time is needed for the bigger particles. Although higher solution treatment temperatures allow shorter disintegration times, they cause rapid expansion of the porosities close to surface of the casting which ends up with blisters. **Figure 5** shows some examples of blister formation for the samples heat treated at 520 and 530 °C.

The Si particle size distributions in as-cast alloys with and without Sr addition are given in Figure 7a. Although most of

the particles for both alloys have a width smaller than 0.45 μm, some coarser particles are also observed. For silicon particles with a radius larger than 0.3 μm, the calculated disintegration time at 470 °C is greater than 2 h. As the required disintegration time for these thicker Si particles is much longer, this caused incomplete spheroidization in some heat treatment conditions and reduced the average circularity (C). Calculated circularity values (Equation (3)) of the silicon particles after different heat treatments are shown in Figure 4, as well as the average silicon particle area. The circularity of a phase in the microstructure is defined as the degree to which the particle is similar to a circle, taking into consideration the smoothness of the periphery. This means circularity is a measurement of both particle form and roughness.

Thus, the further away from a perfectly round, smooth circle a particle becomes, the lower the circularity value.

$$C = \frac{1}{n}\sum_{k=1}^{n}\frac{4\pi A_k}{P_k^2} \qquad (3)$$

The ratio of area (A) and perimeter (P) of Si particle is decisive in the formula, and when circularity value is 1, it indicates a perfect circle, and as it approaches 0, it indicates an increasingly elongated polygon.

It is seen in Figure 4 that the mean eutectic Si particle area is lower, and the circularity is higher for the Sr-modified alloys under all heat treatment conditions. The difference between modified and unmodified alloys is bigger for short heat treatment durations and gets smaller with increased heat treatment time. For a higher heat treatment temperature of 510 °C, the difference between the two alloys is small even at a shorter dwell time of 30 min, and this difference remains constant for longer heat treatment times. In general, 30 min of heat treatment at 510 °C seems sufficient to disintegrate Si coral branches and achieve sufficient Si circularity. The morphological change in the eutectic Si phase after solution heat treatment can be seen in **Figure 6**.
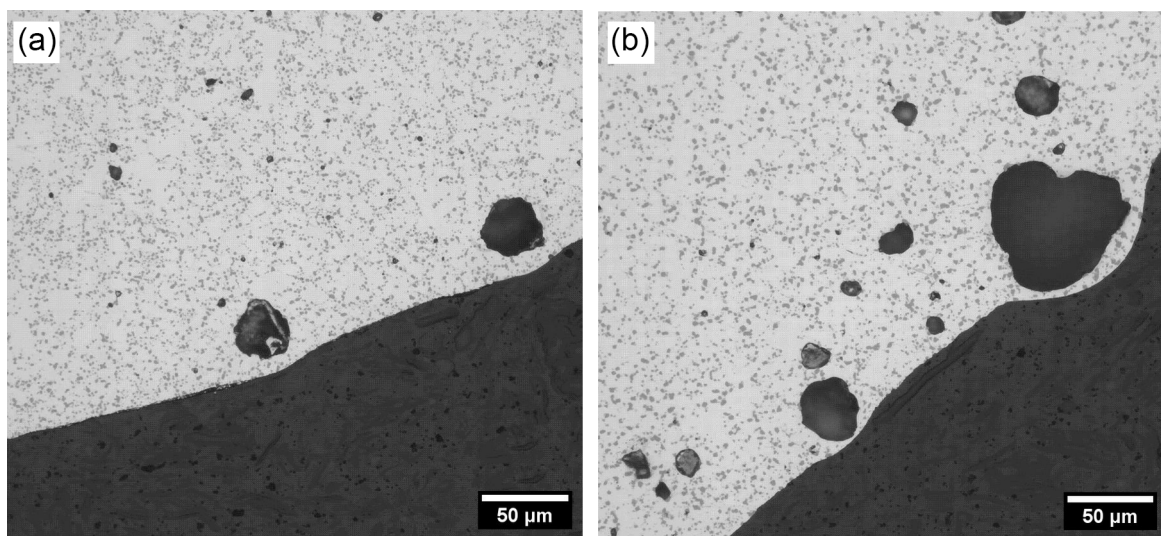
Figure 5. Blister formation on the surface of samples heat treated at a) 520 °C and b) 530 °C.
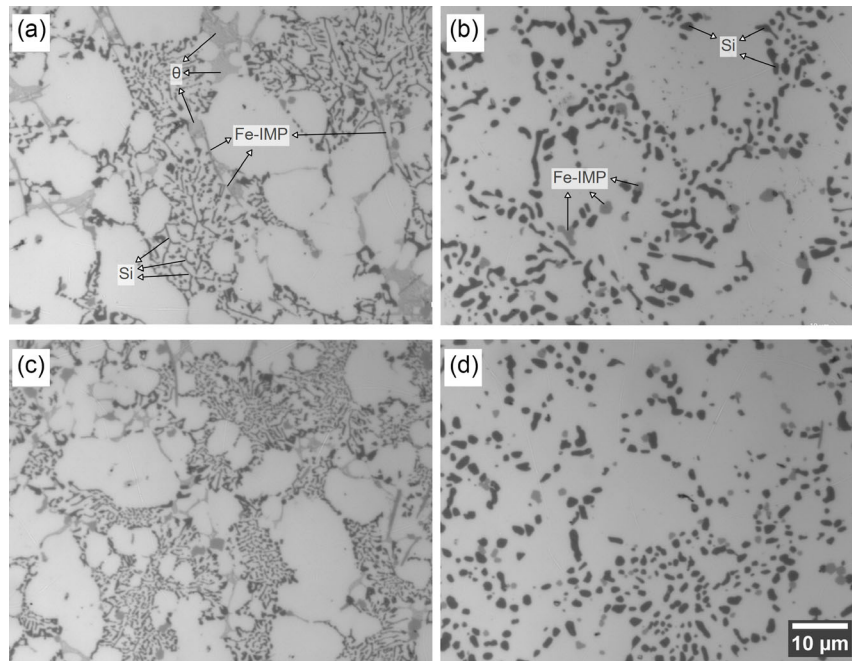
Figure 6. Microstructures of a) A384 and c) A384 + Sr as-cast samples, b) A384, and d) A384 + Sr samples after solution treatment (510 °C-30 min).
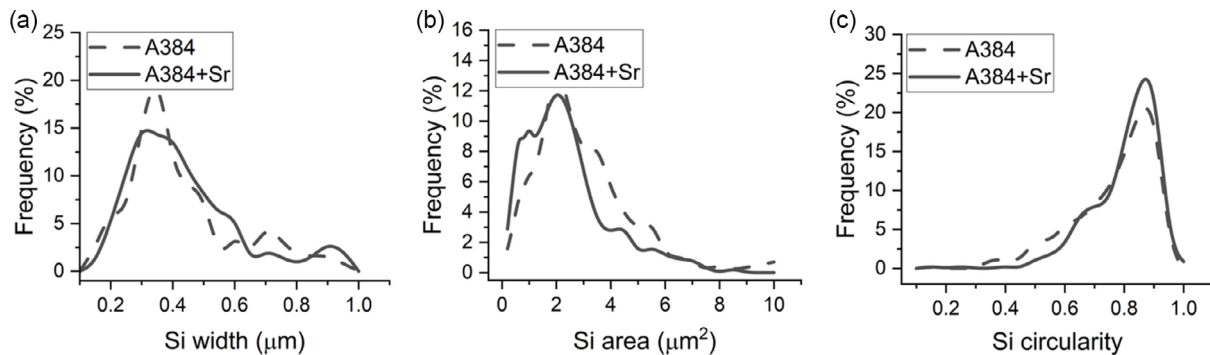
Figure 7. Graphs showing distribution of a) width in as-cast condition, b) area in heat-treated condition (510 °C - 30 min), and c) circularity in heat-treated condition (510 °C - 30 min) of silicon particles.

Particle area distribution and circularity after solution treatment at 510 °C for 30 min are shown in **Figure 7**b,c, respectively. It is well known that modification with Sr changes the eutectic Si morphology from acicular plates to a rounded, fiber-like form.[29] The measured width of the Si particles for both alloys showed a similar distribution, and the mean thicknesses of the silicon particles were 0.45 and 0.47 µm for unmodified and Sr modified alloys, respectively. The small difference between these values is possibly a result of the fast cooling rate achieved in the HPDC process, which refines Si particles. The effect of Sr modification is more prominent after heat treatment, as shown in Figure 7b, where the mean area of Si particles is smaller and the circularity (Figure 7c) is higher for the modified alloy.

Paray et al.[30] also reported that the addition of Sr facilitates the fragmentation and spheroidization processes of Si particles. Spheroidization of the unmodified eutectic Si consists of 1) Si plate fragmentation/disintegration; 2) spheroidization of broken Si particles; and 3) coarsening of Si particles. In step (3), smaller Si particles are dissolved at the expense of the growth of larger particles, thereby causing an increase in the average particle size.[31] Morphological changes of the silicon particles during heat treatment are schematically shown in **Figure 8**. The process of spheroidization and coarsening is different for modified and unmodified alloys. For unmodified alloys, the first step is the fragmentation of the needle-like particles, which is followed by spheroidization. For the modified alloys, silicon particles already have a refined morphology, and spheroidization commences shortly after the solution treatment is underway.

The Ostwald ripening behavior of the precipitates during isothermal annealing has been described by Lifshitz, Slyozov, and Wagner (so called LSW theory)[32,33] and it predicts that the average particle radius, r, should increase with time, t, according to Equation (4).
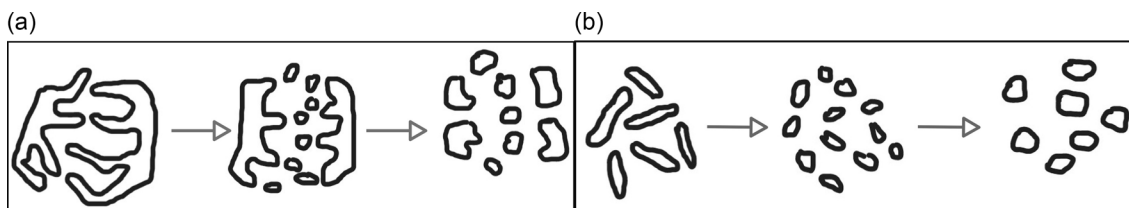
Figure 8. Change of eutectic Si particle morphology during solution heat treatment in a) unmodified and b) modified Al–Si casting alloys.

$$r_t^n - r_{t_0}^n = k_r t \tag{4}$$

where r is the average radius of the Si precipitates at time t and t_0, n is the coarsening exponent, k_r is the rate constant including lattice diffusivity, and t is the annealing time. In the typical LSW theory, the value of n is equal to 3, which means that the coarsening process is controlled by the volume diffusion.

A series of experiments were conducted to investigate the coarsening behavior of silicon particles as a function of heat treatment time for different heat treatment temperatures. Si sizes after different heat treatments were measured using image analysis. The measured Si size was converted to an equivalent diameter to calculate average radius values. The equivalent circular diameter, or area-equivalent diameter, is defined as the diameter of a circle with the same area as the particle. Thus, once the area of the particle, A, has been measured, the area-equivalent radius (r_e) can be calculated using Equation (5).[34]

$$r_e = \frac{1}{l} \sum_{k=1}^{l} \sqrt{\frac{A_k}{\pi}} \tag{5}$$

For better understanding of the variation of the coarsening exponent, the relationship between r and t is shown in **Figure 9**a for different solution treatment temperatures. All of the experimental data exhibit a good linear relationship with $n \approx 3$. k_r for samples at various solution temperatures are compared in Figure 9b. As shown in the graphs, the value of k_r is larger for unmodified alloys for all tested heat treatment temperatures, which means coarsening is faster for these alloys. The

reason for this behavior could be related to the size distribution of Si particles in the unmodified and modified alloys. For the unmodified alloy, large silicon particles coexist with much smaller ones. This size difference causes smaller ones to dissolve and provide the flux of silicon atoms for the growth of the bigger ones at a faster rate compared to the modified alloys where the size distribution is much narrower. Another parameter could be the shape of the particles; the acicular shape of the silicon particles in unmodified alloy creates a driving force for them to grow and get more circular.

Apart from silicon spheroidization, another important result of the solution heat treatment is the dissolution of the intermetallic phases in the microstructure of the as-cast material. Because dissolution of these secondary phases is a diffusion-controlled process, heat treatment temperature and duration are critical parameters. As a rule, higher temperatures and longer durations provide increased dissolution. However, higher temperatures and prolonged heat treatments can cause problems like blistering and grain coarsening, so finding optimum conditions for solution heat treatment is critical.

The main intermetallic phases in the current alloy that can be dissolved during solution heat treatment and then precipitate during aging are Al_2Cu (θ) and $Al_5Cu_2Mg_8Si_6$ (Q) phases.[35,36] **Figure 10** shows formation temperatures and fractions of the phases in the studied alloy as well as the fractions of Q and θ phases at different temperatures under equilibrium conditions calculated using Thermo-Calc software. As expected with increased temperature, the amount of intermetallics decreases. When the temperature is 510 °C, all of the Q phase is dissolved,
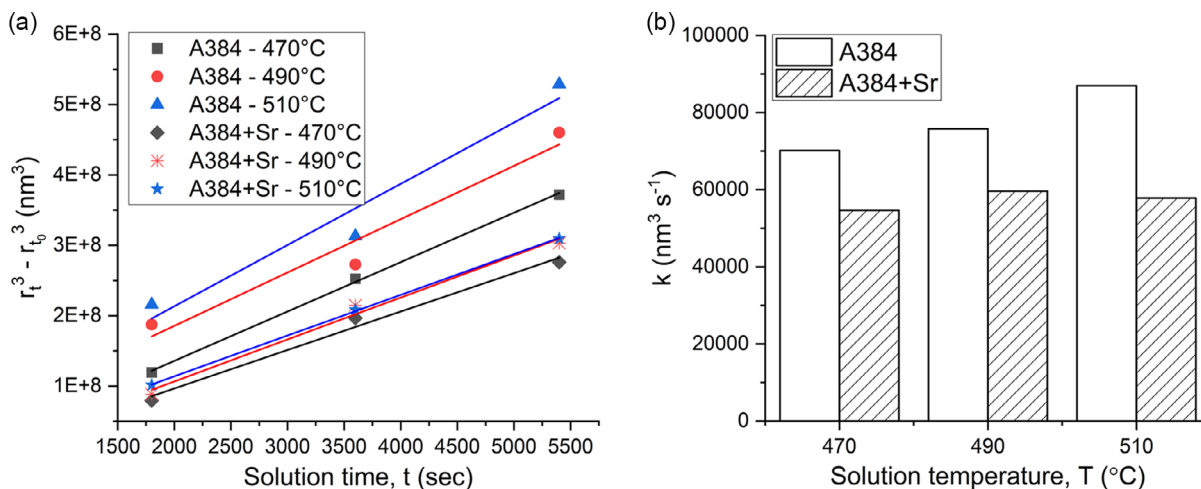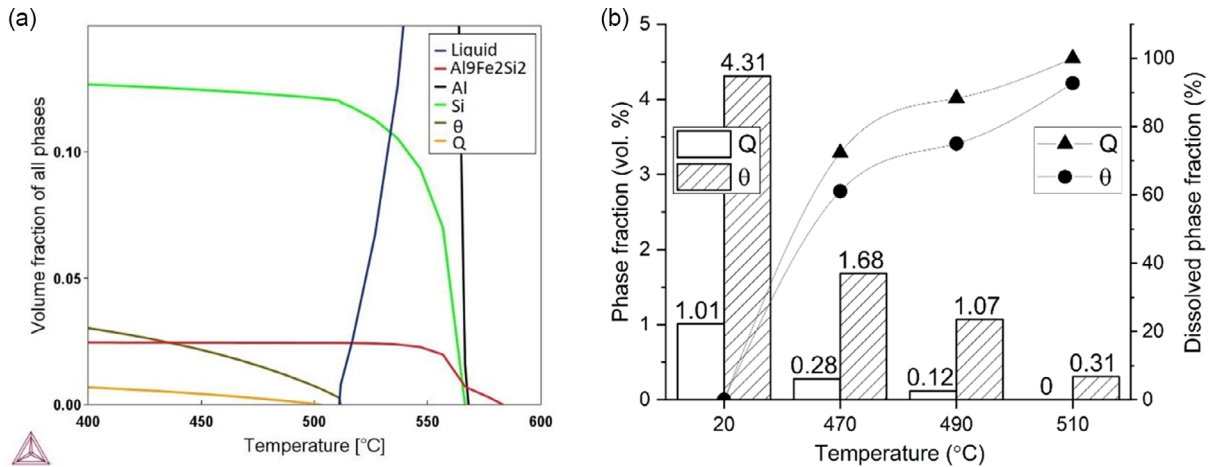

Figure 9. Change of a) equivalent radius versus solution time and b) coarsening parameter k against solution temperature.

Figure 10. Thermodynamic modeling of the a) change of phase fractions with temperature and b) equilibrium phase fractions of θ and Q at different solution temperatures.

and only around 7% of the θ phase remains undissolved. Quick dissolution of θ and Q phases has already been reported in the literature, where most of the Al_2Cu was dissolved and the amount of Mg dissolved in α-Al was more than doubled even after 10 min at 495 °C.[37] Although further increasing the temperature would help to dissolve remaining intermetallics, it could result in incipient melting.[38,39]

After evaluation of the results of silicon particle circularity/ size and dissolution of intermetallic phases, two different solution heat treatment procedures were selected for further investigation, 30 min at 490 °C and 30 min at 510 °C. Polished cross sections of the heat-treated samples were investigated with an OM to see if there was any blistering problem on their surfaces. All of the samples were free of blistering.

3.3. Aging

After the solution treatments at two different temperatures (490 and 510 °C), the samples were aged naturally at room

temperature and artificially at 170 and at 190 °C. For natural aging, solution-treated samples were kept at room temperature for 14 days (T4 treatment) and then tensile tests were carried out. The radar chart with the average values of tensile test results as well as hardness is shown in **Figure 11**a. The aging curves at 170 and 190 °C are shown in Figure 11b for samples that are solution treated at two different temperatures (490 and 510 °C).

As shown in Figure 11a, solution heat treatment at 490 °C results in higher strength and lower elongation after T4 treatment; on the other hand, the hardness values of the samples heat treated at both temperatures are very similar. The reason for high strength of the samples solution treated at 490 °C is related to the amount of intermetallics that dissolve during heat treatment. As shown in Figure 10b, solution treatment at 490 °C results in a higher content of undissolved intermetallics in the microstructure compared to solution treatment at 510 °C. The existence of these intermetallics contributes to increased strength of the material but causes a lower ductility due to their brittle nature. Although solution treatment at 510 °C dissolves most of the
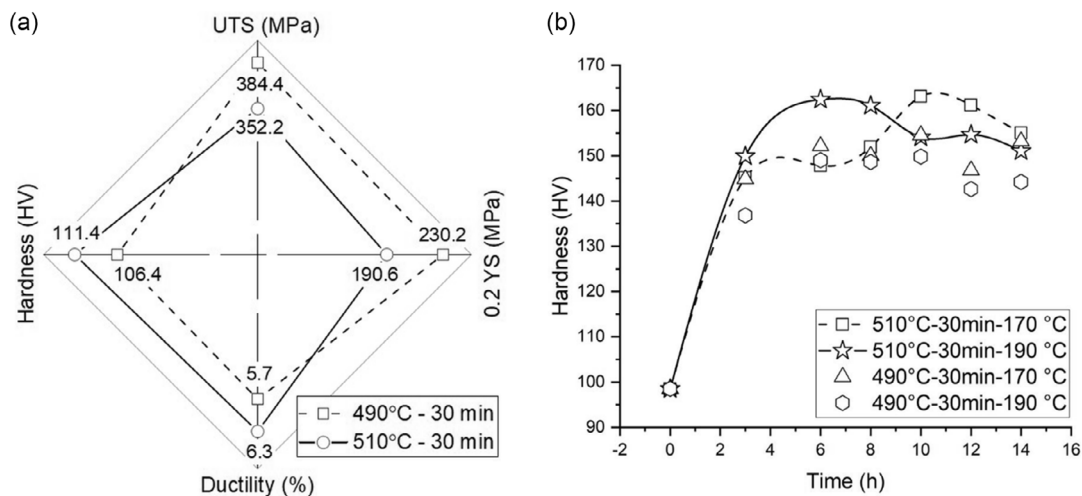
Figure 11. a) Mechanical properties after T4 treatment and b) aging curves after different solution treatments of A384 alloy.

2301196 (7 of 9)
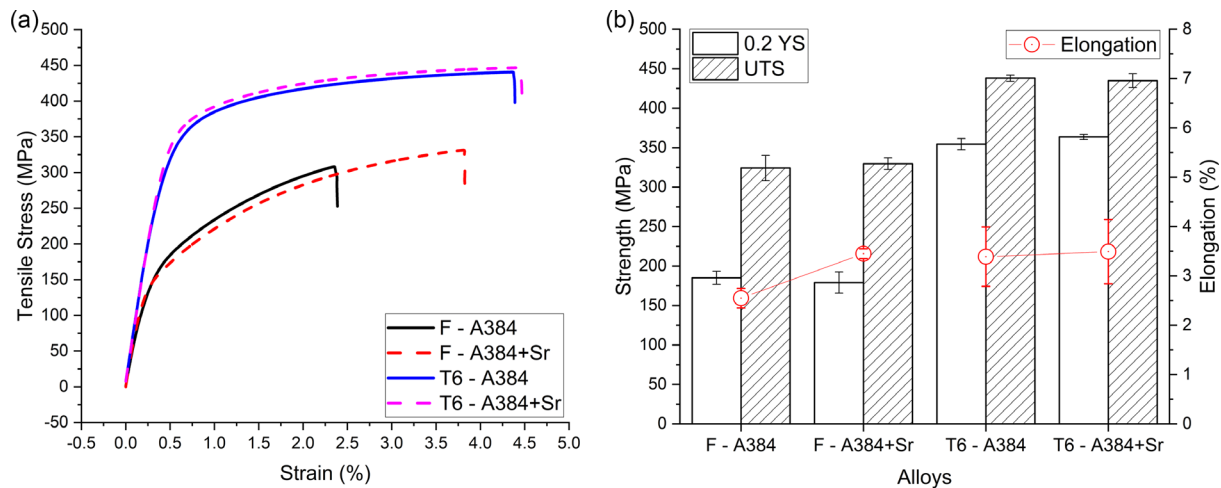
Figure 12. Tensile properties of as-cast and heat-treated samples.

intermetallic phases, solution strengthening and formation of precipitates at room temperature are not enough to cause higher strength.

In the case of artificial aging, atoms have high mobility because of the increased aging temperature and formation of precipitates is easier. In the case of artificial aging, the amount of dissolved atoms plays an important role in the final strength of the material. Figure 11b shows the change of hardness with aging time for different solution and aging treatment temperatures. For both aging temperatures, maximum hardness is achieved by the samples solution treated at 510 °C. Increasing aging temperature from 170 to 190 °C results in a shorter time requirement for peak hardness, but the peak hardness values for both aging temperatures are almost the same.

After evaluation of the tensile properties of the T4-treated materials and aging curves of the T6-treated samples, the optimum heat treatment for improved strength for this alloy was selected as solution treatment at 510 °C for 30 min + water quenching + aging at 190 °C for 6 h.

Tensile bars of A384 and A384 + Sr alloys were heat treated according to the selected recipe and tested at room temperature. The results of these tensile tests are given in **Figure 12**.

For both alloys, the selected T6 heat treatment resulted in tensile strength of 435 MPa, to the best of the current authors' knowledge and the compiled data shown in Figure 1, this is the highest reported value for this alloy. The T6 heat treatment increased yield strength from 185 to 354 MPa (91% increase) and 179 to 363 MPa (102% increase) for A384 and A384 + Sr alloys, respectively. The average elongation at break is around 3.5% (42% increase) for both alloys.

4. Conclusions

The results of the current study show that with tailored heat treatments, it is possible to improve the mechanical properties of the HPDC Al–Si–Cu–Mg alloys. The data show that solution treatment at 510 °C for 30 min provides disintegration and spheroidization of eutectic Si particles with the sufficient dissolution of

intermetallic phases. Calculated disintegration time using the average Si particle radius is in good agreement with the experimental results. Experiments show that coarsening of Si particles happens faster for unmodified alloys, which is a result of the coexistence of different sized particles. The effect of Sr addition on the circularity of Si particles is more prominent in the as-cast condition. After 30 min of solution treatment at 510 °C and 6 h of aging at 190 °C, yield strength and ultimate tensile strength values above 360 and 430 MPa were recorded, respectively. A comparison of the tensile data for modified and unmodified alloys shows that although the addition of Sr increases the ductility of the material in the as-cast state, it has almost no effect on the mechanical properties of heat-treated samples. OM conducted on the polished cross sections of the heat-treated samples showed no signs of blister formation. The optimal heat treatment conditions presented here provide an opportunity for HPDC foundries to further enhance mechanical properties without changing the alloy composition or casting parameters.

Conflict of Interest

The authors declare no conflict of interest.

Data Availability Statement

The data that support the findings of this study are available from the corresponding author upon reasonable request.

Keywords

[1] W. Khalifa, Y. Tsunekawa, M. Okumiya, *J. Mater. Process Technol.* **2010**, *210*, 2178.

[2] Y. Sui, Q. Wang, G. Wang, T. Liu, *J. Alloys Compd.* **2015**, *622*, 572.

[3] D. Li, C. Cui, X. Wang, Q. Wang, C. Chen, S. Liu, *Mater. Des.* **2016**, *90*, 820.

[4] P. Zhang, Z. Li, B. Liu, W. Ding, *Mater. Sci. Eng., A* **2016**, *661*, 198.

[5] B. Zhao, B. Ye, L. Wang, Y. Bai, X. Yu, Q. Wang, W. Yang, *Mater. Sci. Eng., A* **2022**, *849*, 143463.

[6] T. Liu, S. Morales, M. Karkkainen, L. Nastac, V. Arvikar, I. Levin, L. N. Brewer, *Mater. Sci. Eng., A* **2019**, *756*, 373.

[7] R. N. Lumley, R. G. Odonnell, D. R. Gunasegaram, M. Givord, *Metall. Mater. Trans. A* **2007**, *38*, 2564.

[8] Q. Cai, C. L. Mendis, I. T. H. Chang, Z. Fan, *Mater. Sci. Eng., A* **2021**, *800*, 140357.

[9] I. Outmani, L. Fouilland-Paille, J. Isselin, M. El Mansori, *J. Mater. Process Technol.* **2017**, *249*, 559.

[10] S. K. Chaudhuryand, D. Apelian, *Metall. Mater. Trans. A* **2006**, *37A*, 2295.

[11] L. Lasa, J. M. Rodriguez-Ibabe, *J. Mater. Sci.* **2004**, *39*, 1343.

[12] E. Sjölander, S. Seifeddine, *J. Mater. Process Technol.* **2010**, *210*, 1249.

[13] X. Liu, B. Beausir, Y. Zhang, W. Gan, H. Yuan, F. Yu, C. Esling, X. Zhao, L. Zuo, *J. Alloys Compd.* **2018**, *730*, 208.

[14] Z. Li, N. Limodin, A. Tandjaoui, P. Quaegebeur, D. Balloy, *Mater. Charact.* **2021**, *173*, 110919.

[15] A. M. Samuel, H. W. Doty, S. Valtierra, F. H. Samuel, *Mater. Des.* **2013**, *52*, 947.

[16] F. H. Samuel, *J. Mater. Sci.* **1998**, *33*, 2283.

[17] G. Eisaabadi B., G. Y. Yeom, M. Tiryakioğlu, N. Netto, R. Beygi, M. Z. Mehrizi, S. K. Kim, *Mater. Sci. Eng., A* **2018**, *722*, 1.

[18] G. K. Sigworth, R. J. Donahue, *Int. J. Metalcast.* **2021**, *15*, 1031.

[19] B. Dybowski, A. Kielbus, L. Poloczek, *Eng. Failure Anal.* **2023**, *150*, 107223.

[20] H. Demirtaş, E. Karakulak, N. H. Babu, *J. Alloys Compd.* **2022**, *896*, 163111.

[21] A. R. Farkoosh, M. Pekguleryuz, *Mater. Sci. Eng., A* **2015**, *621*, 277.

[22] X. Zhu, X. Dong, P. Blake, S. Ji, *Mater. Sci. Eng., A* **2021**, *802*, 140612.

[23] E. Vandersluis, B. Andilab, C. Ravindran, M. Bamberger, *Mater. Charact.* **2020**, *167*, 110499.

[24] I. Sadeghi, M. A. Wells, S. Esmaeili, *Mater. Des.* **2017**, *128*, 241.

[25] G. Timelli, O. Lohne, L. Arnberg, H. I. Laukli, *Metall. Mater. Trans. A* **2008**, *39*, 1747.

[26] X. Dong, H. Youssef, Y. Zhang, H. Yang, S. Wang, S. Ji, *Mater. Des.* **2020**, *186*, 108372.

[27] S. Joseph, S. Kumar, *Mater. Sci. Eng., A* **2013**, *588*, 111.

[28] E. Ogris, A. Wahlen, H. Lüchinger, P. J. Uggowitzer, *J. Light Met.* **2002**, *2*, 263.

[29] M. A. Moustafa, F. H. Samuel, H. W. Doty, *J. Mater. Sci.* **2003**, *38*, 4523.

[30] F. Paray, J. E. Gruzleski, *Cast Met.* **1992**, *5*, 187.

[31] A. M. Samuel, M. H. Abdelaziz, H. W. Doty, F. H. Samuel, *Int. J. Metalcast.* **2022**, *16*, 1709.

[32] I. M. Lifshitz, V. V. Slyozov, *J. Phys. Chem. Solids* **1961**, *19*, 35.

[33] C. Wagner, *Z. Elektrochem.* **1961**, *65*, 581.

[34] J. L. Colley, PhD Thesis, The University of British Columbia **2011**.

[35] Y. N. Piao, H. L. Jia, M. Zha, P. K. Ma, D. Gao, C. R. Yin, Z. Z. Yang, H. Y. Wang, *Mater. Charact.* **2023**, *196*, 112609.

[36] A. Fabrizi, S. Capuzzi, A. De Mori, G. Timelli, *Metals* **2018**, *8*, 750.

[37] E. Sjölander, S. Seifeddine, *Metall. Mater. Trans. A* **2014**, *45*, 1916.

[38] A. Lombardi, C. Ravindran, R. MacKay, *Mater. Sci. Eng., A* **2015**, *633*, 125.

[39] Y. Han, A. M. Samuel, H. W. Doty, S. Valtierra, F. H. Samuel, *Mater. Des.* **2014**, *58*, 426.

[40] H. Yang, S. Ji, W. Yang, Y. Wang, Z. Fan, *Mater. Sci. Eng., A* **2015**, *642*, 340.

[41] R. Doglione, P. Di Geronimo, A. Morano, *Am. J. Appl. Sci.* **2021**, *12*, 64.

[42] R. Lumley, *Mater. Sci. Forum* **2011**, *693*, 247.

[43] R. N. Lumley, D. Viano, J. R. Griffiths, C. J. Davidson, in *Proc. 12th Inter. Conf. on Aluminium Alloys* (Eds: S. Kumai, O. Umezawa, Y. Takayama, T. Tsuchida, T. Sato), JILM, Yokohoma **2010**.

[44] R. N. Lumley, I. J. Polmear, P. R. Curtis, *Metall. Mater. Trans. A* **2009**, *40*, 1716.

[45] R. B. C. Cayless, *ASM Handbook Vol. 2: Properties And Selection: Nonferrous Alloys And Special-Purpose Materials*, ASM International, OH, USA **1990**, Ch. 1.